Article

Two-dimensional supersolidity in a dipolar quantum gas

Matthew A. Norcia[1,4], Claudia Politi[1,2,4], Lauritz Klaus[1,2], Elena Poli[2], Maximilian Sohmen[1,2], Manfred J. Mark[1,2], Russell N. Bisset[2], Luis Santos[3] & Francesca Ferlaino[1,2✉]

Supersolid states simultaneously feature properties typically associated with a solid and with a superfluid. Like a solid, they possess crystalline order, manifesting as a periodic modulation of the particle density; but unlike a typical solid, they also have superfluid properties, resulting from coherent particle delocalization across the system. Such states were initially envisioned in the context of bulk solid helium, as a possible answer to the question of whether a solid could have superfluid properties[1–5]. Although supersolidity has not been observed in solid helium (despite much effort)[6], ultracold atomic gases provide an alternative approach, recently enabling the observation and study of supersolids with dipolar atoms[7–16]. However, unlike the proposed phenomena in helium, these gaseous systems have so far only shown supersolidity along a single direction. Here we demonstrate the extension of supersolid properties into two dimensions by preparing a supersolid quantum gas of dysprosium atoms on both sides of a structural phase transition similar to those occurring in ionic chains[17–20], quantum wires[21,22] and theoretically in chains of individual dipolar particles[23,24]. This opens the possibility of studying rich excitation properties[25–28], including vortex formation[29–31], and ground-state phases with varied geometrical structure[7,32] in a highly flexible and controllable system.

Ultracold atoms have recently provided a fundamentally new direction for the creation of supersolids—rather than looking for superfluid properties in a solid system such as [4]He, ultracold atoms allow one to induce a crystalline structure in a gaseous superfluid, a system that provides far greater opportunity for control and observation. This new perspective has enabled supersolid properties to be observed in systems with spin–orbit coupling[33] or long-range cavity-mediated interactions[34], though in these cases the crystalline structure is externally imposed, yielding a state with a rigid lattice, and hence no phononic excitations. In contrast, dipolar quantum gases of highly magnetic atoms can spontaneously form crystalline structure due to intrinsic interactions[11–13], allowing for a supersolid with both crystalline and superfluid excitations[14–16]. In these demonstrations, supersolid properties have been observed only along a single dimension, as a linear chain of phase-coherent 'droplets', that is, regions of high density connected by low-density bridges of condensed atoms, confined within an elongated optical trap. Compared with previous studies of incoherent two-dimensional (2D) dipolar droplet crystals[8,35], we work with both a substantially higher atom number N and relatively strong repulsive contact interactions between atoms. This leads to the formation of large numbers of loosely bound droplets, enabling both phase coherence and modulation along two dimensions. In our system, the repulsive dipolar interactions between droplets facilitate a structural transition from linear arrays to arrays with transverse structure, analogous to the Coulomb-interaction-mediated structural phase transitions observed with ions[17–20]. Unlike ions however, our droplets are compressible and result from the spontaneous formation of a density wave, allowing for dynamical variation in both droplet number and size. Further, the exchange of particles between droplets enables the spontaneous synchronization of the internal phase of each droplet across the system, and the associated superfluid excitations[14–16].

Calculated ground-state phase diagram

Dipolar quantum gases show a rich set of ground- and excited-state phenomena owing to the competition between many energetic contributions. These include mean-field interactions of both contact and dipolar nature, quantum fluctuations, and external confinement, parameterized by potentially anisotropic trapping frequencies $f_{x,y,z}$. Such systems can be described with great accuracy by using an extended Gross–Pitaevskii equation (eGPE)[36–39]. Even a fine variation of the strength of these energetic contributions can lead to dramatic qualitative changes in the state of the system, for example, enabling a transition from a uniform condensate to a supersolid, or in our present case, from linear to 2D supersolidity.

Figure 1a shows ground-state density profiles calculated across this transition using the eGPE at zero temperature. These profiles feature arrays of high-density droplets, immersed in a low-density coherent 'halo' that establishes phase coherence across the system. For highly elongated traps, the ground state is a linear chain of phase-coherent
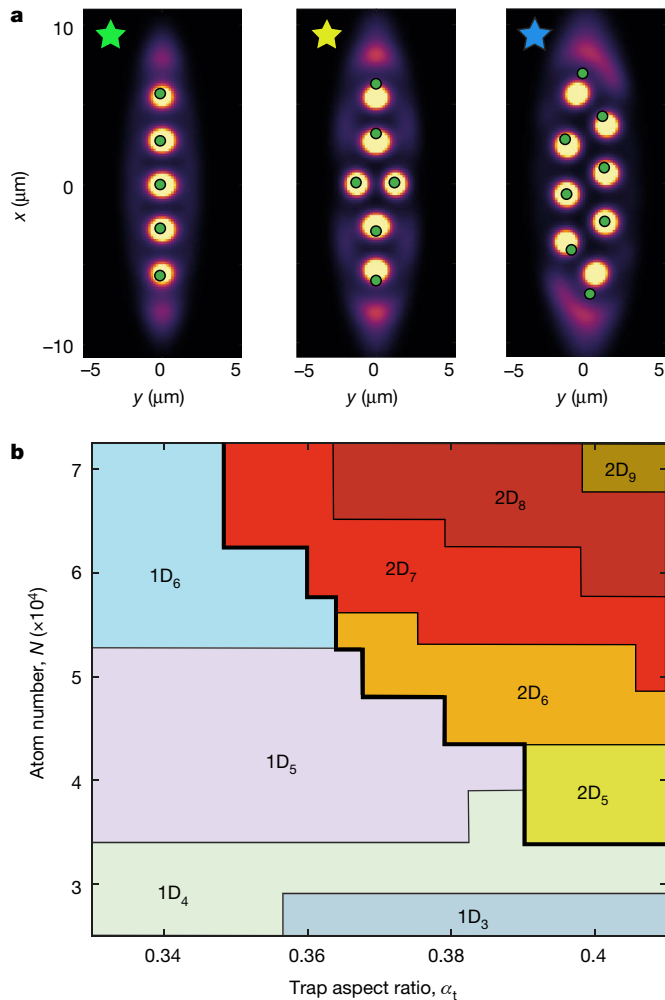
Fig. 1 | Calculated phases of dipolar droplet array. a, In-trap ground-state density profiles calculated using eGPE for atom numbers $N \in [3.3, 4.4, 5.8] \times 10^4$ in the droplets and trap aspect ratios $\alpha_t = f_x/f_y \in [0.33, 0.35, 0.39]$ (left to right). The scattering length $a = 88a_0$, where a_0 is the Bohr radius. The green dots depict the droplet positions obtained from the variational model, assuming the same N and droplet number N_D as the eGPE. The stars relate to the experimentally observed density profiles in Fig. 2b. **b**, Phase diagram, obtained from our variational model, as a function of N and α_t for $f_x = 33$ Hz and $f_z = 167$ Hz. Linear (2D) phases with N_D droplets are labelled as $1D_{N_D}$ ($2D_{N_D}$).

droplets. For traps that are more round, the ground state develops transverse structure, acquiring modulation along two directions. Further changes in trap parameters produce states with additional rows, eventually reaching an isotropic condition for round traps (see Methods for theoretical and experimental demonstration). For simplicity, we refer to all droplet arrays with transverse modulation as 2D, by which we do not imply isotropic 2D periodic character.

Although the eGPE has remarkable predictive power, full simulations in three dimensions are numerically intensive, making a global survey of the array properties as a function of our experimental parameters difficult. To overcome this limitation, we employ a variational ansatz that captures the key behaviour of the system, and allows us to disentangle the competing energetic contributions. In this approach, we describe an array of N_D droplets by the wavefunction $\psi(\mathbf{r}) = \sum_{j=1}^{N_D} \psi_j(\mathbf{r})$, where the jth droplet is assumed to be of the form: $\psi_j(\mathbf{r}) \propto \sqrt{N_j} \exp\left(-\frac{1}{2}\left(\frac{|\rho - \rho_j|}{\sigma_{\rho,j}}\right)^{r_{\rho,j}}\right) \exp\left(-\frac{1}{2}\left(\frac{|z - z_j|}{\sigma_{z,j}}\right)^{r_{z,j}}\right)$, interpolating between a Gaussian and a flat-top profile characteristic of quantum droplets[40]. For a given total number of atoms N and droplet

number N_D, energy minimization provides the atom number N_j in each droplet, as well as their widths $\sigma_{\rho(z),j}$, exponents $r_{\rho(z),j}$ and positions $\rho_j = (x_j, y_j)$. Repeating this energy minimization as a function of N_D gives the optimal number of droplets. This model provides a good qualitative description of the overall phase diagram (Fig. 1b), revealing that the interplay between intradroplet physics and interdroplet interaction results in a rich landscape of structural transitions as a function of the atom number and the trap aspect ratio $\alpha_t = f_x/f_y$.

Several trends are immediately visible from the phase diagram. Larger N and higher α_t generally produce states with larger numbers of droplets. Further, as with ions, a large number of droplets favours a 2D configuration, while tighter transverse confinement (small α_t) favours a 1D configuration[17–20]. A transition from 1D to 2D is thus expected when moving towards larger N or to higher α_t. In stark contrast to the case of ions, the number of droplets typically increases across the 1D-to-2D transition, whereas only narrow regions in the phase diagram may allow for a 1D-to-2D transition at constant droplet number.

The variational results are in excellent agreement with our eGPE numerics, in terms of predicting the qualitative structure of droplet array patterns, as shown in Fig. 1a. Slight discrepancies exist between the two theories regarding the predicted droplet positions and the location of the 1D-to-2D transition. This is probably because of the presence of the halo in the eGPE simulation (and presumably in the experiment), visible in Fig. 1a, which is not accounted for in the variational model. This halo appears to accumulate at the ends of the trap, pushing the droplets towards the trap centre and probably increasing the effective trap aspect ratio experienced by the droplets.

In-trap density distributions in experiment

To explore the 1D-to-2D transition experimentally, we use a condensate of highly magnetic ^{164}Dy atoms confined within an anisotropic optical dipole trap with independently tunable trap frequencies $f_{x,y,z}$. The trap, shown in Fig. 2a, is shaped like a surfboard with the tight axis along gravity and along a uniform magnetic field that orients the atomic dipoles and allows tuning of the contact interaction strength. Typically, we perform evaporation directly into our state of interest at our desired final interaction strength and trap parameters, as demonstrated in refs. [13,41]. This avoids excitation of the system, as can occur during an interaction quench. A combination of in-trap and time-of-flight (TOF) imaging provides us with complementary probes of the density profile of our atomic states, and the phase coherence across the system.

We begin by studying the transition from 1D to 2D by changing the strength of the transverse confinement provided by the trap between subsequent runs of the experiment. Our optical setup allows us to tune f_y from roughly 75 Hz to 120 Hz, while leaving f_x and f_z nearly constant at 33(2) Hz and 167(1) Hz, and thus to vary the trap aspect ratio α_t in the plane perpendicular to the applied magnetic field and our imaging axis. For small α_t, the atoms are tightly squeezed transversely, and form a linear-chain supersolid (as seen in in-trap images of Fig. 2b). For α_t above a critical value $\alpha_t^* = 0.34(2)$, we observe a structural phase transition to a 2D state with two side-by-side droplets in the centre of the chain. By further increasing α_t, the 2D structure extends to two offset lines of droplets in a zigzag configuration. The observed patterns match well with the ground-state predictions from the eGPE calculations when we globally fix the scattering length to $88a_0$, where a_0 is the Bohr radius. Further modifications of the trap parameters can produce droplet arrays with more than two rows, as shown in Fig. 2d, Extended Data Fig. 2.

We obtain higher atom numbers in the more oblate traps (higher α_t), giving $N = 6.5(5) \times 10^4$ at $\alpha_t = 0.44$ and $N = 2.5(4) \times 10^4$ at $\alpha_t = 0.28$. This further facilitates the crossing of the 1D-to-2D transition, by favouring states with larger numbers of droplets in the broader traps. In the 2D regime, modulation is clearly visible for durations beyond one second.
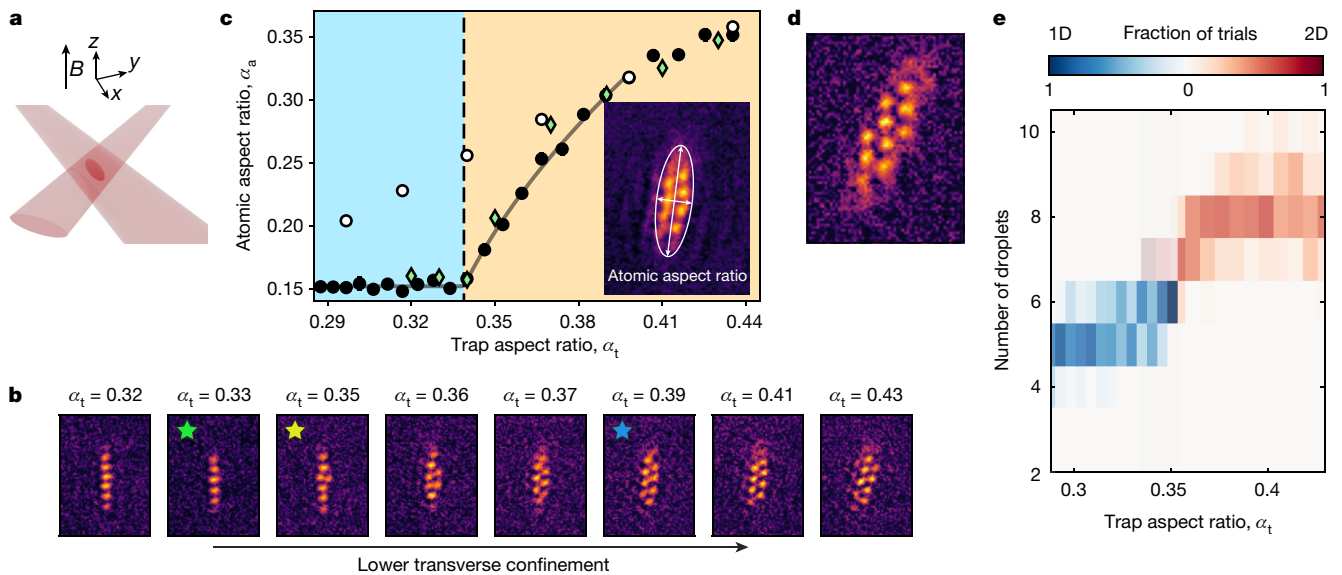
Fig. 2 | Linear to zigzag transition in an anisotropic trap. a, We confine and condense dipolar [164]Dy atoms within an anisotropic ODT formed by the intersection of two laser beams. By tuning the aspect ratio of the trap in the x–y plane (α_t), perpendicular to an applied magnetic field **B**, we induce a transition between linear and zigzag configurations of droplets. **b**, Single-trial images of the in-trap density profile of atoms at different α_t, showing the structural transition from linear to zigzag states, as well as an increase in droplet number for higher α_t. The stars indicate values α_t and N corresponding to the eGPE calculations of Fig. 1a. **c**, Atomic aspect ratio α_a versus trap aspect ratio α_t for the dataset of **b**. α_a is the ratio of minor to major axes of a 2D Gaussian fit to the imaged in-trap density profile (inset). For the supersolid droplet array (black markers), we see an abrupt change in α_a at the critical trap aspect ratio α_t^*,

extracted from the fit (grey line; see Methods). The shape of the transition agrees well with eGPE prediction (green diamonds; see Methods). For an unmodulated condensate (white markers), no abrupt change is evident. The error bars represent the standard error on the mean over approximately 20 trials, and are smaller than the markers on most points. **d**, Reducing trap confinement at a trap aspect ratio of $\alpha_t = 0.4(1)$ enables the creation of states with more than two rows (Extended Data Fig. 2). **e**, Distribution of droplet number versus α_t, showing a distinct increase in droplet number at the transition from linear to zigzag configurations. The saturation of the colour scale corresponds to the fraction of trials with a given droplet number, with blue (red) indicating 1D (2D) configurations for individual trials.

This long lifetime is a useful feature for future studies of excitation dynamics. Further, the droplet configuration patterns are fairly repeatable, with clear structure visible in averaged images as shown in the inset of Fig. 2c, which is an average of 23 trials taken over roughly two hours.

The transition from 1D to 2D is immediately visible when plotting the atomic aspect ratio α_a versus α_t, as shown in Fig. 2c. We find that α_a undergoes a rapid change at α_t^*, as the single linear chain develops 2D structure. For comparison, we plot α_a measured for an unmodulated Bose–Einstein condensate, formed at a different magnetic field, which does not feature the sharp kink present for the supersolid state.

In Fig. 2e, we show the number of droplets present for different α_t. In the 1D regime, we typically see between five and six droplets. For $\alpha_t > \alpha_t^*$, this number increases up to an average value of eight droplets at our maximum α_t. Although some of this increase can be associated with the larger N achieved at a higher aspect ratio, we expect from theory (Fig. 1) that changes in the configuration of droplets are typically accompanied by a change in droplet number even at a fixed atom number.

Evidence of phase coherence

The measurements of in-trap density presented above inform us about the structural nature of the transition, but not about phase coherence, which is the key distinguishing feature between an incoherent droplet crystal and a supersolid. Previous observations of 2D droplet arrays[35] were performed in traps where the ground state is a single droplet[8], and the observed droplet crystal was probably a metastable state lacking interdroplet phase coherence. In contrast, we expect from our theoretical calculations that the 2D array is the ground state of our surfboard-shaped trap (for $\alpha_t > \alpha_t^*$), facilitating the formation of a phase-coherent, and therefore supersolid, state for our experimental parameters.

We experimentally demonstrate the supersolid nature of our 2D modulated state using a matter-wave interference measurement, as previously used in linear supersolid chains[11–13] (Fig. 3a). In this measurement, an array of uniformly spaced droplets creates an interference pattern with a spatial period proportional to the inverse of the in-trap droplet spacing. The relative internal phase of the droplets determines both the contrast and spatial phase of the interference pattern[42]. When averaging over many interference patterns, obtained on separate runs of the experiment, clear periodic modulation persists for phase-coherent droplets, but averages out if the relative droplet phases vary between experimental trials. Thus, the presence of periodic modulation in an average TOF image provides a clear signature of supersolidity in our system, as it indicates both periodic density modulation and phase coherence.

Figure 3a shows an example of such an averaged interference pattern for a linear chain. Uniaxial modulation is clearly present along the direction of the chain, indicating a high degree of phase coherence. For comparison, we also show the expected interference pattern calculated for a linear array of four droplets from free-expansion calculations, showing similar structure.

For conditions where in-trap imaging shows a 2D zigzag structure, the averaged interference pattern exhibits clear hexagonal symmetry (Fig. 3b). This is consistent with our expectation, and is indicative of the triangular structure of the underlying state. Because we evaporate directly into the final trap conditions, the phase coherence we observe in both 1D and 2D configurations must form during the evaporative process, indicating a mechanism for establishing phase coherence between droplets[41]. This is in contrast to protocols involving a dynamical ramp of interaction strength or trap parameters, where coherence may be inherited from a pre-existing phase-coherent state. To confirm that the observed modulation is not present without phase coherence, we repeat the measurement of Fig. 3b at a magnetic field corresponding
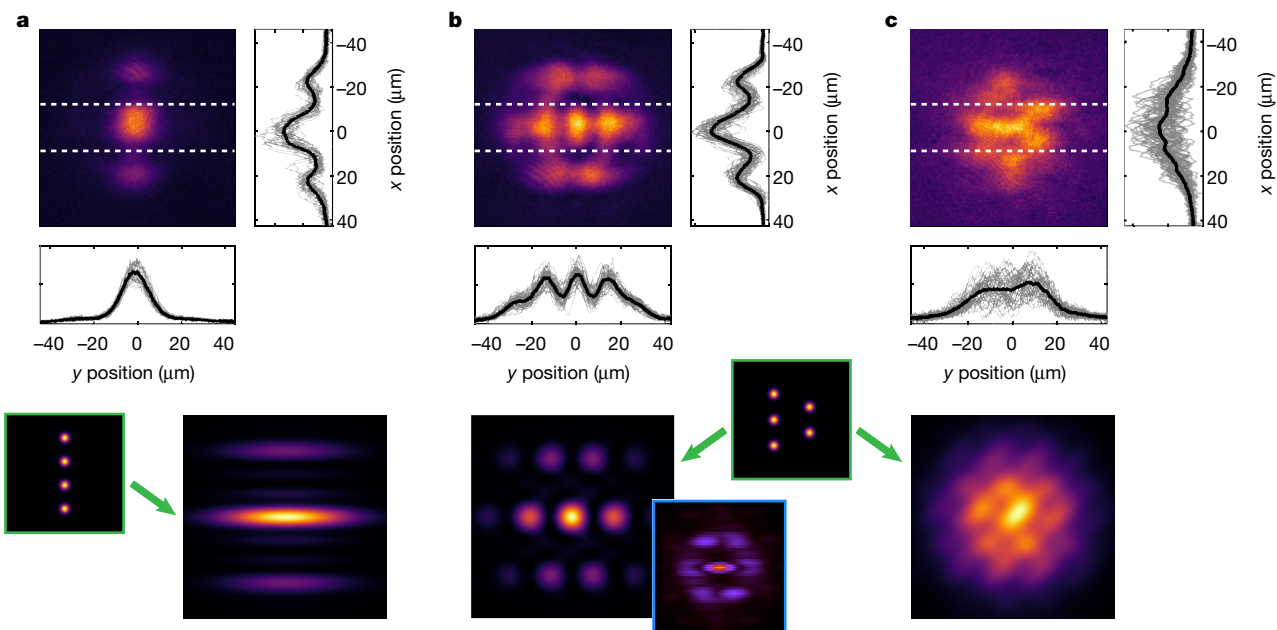
Fig. 3 | Coherence in linear and zigzag states. The upper panels show averaged images of experimental TOF interference patterns, along with projections along the horizontal and vertical directions of average (solid black lines) and individual images (grey lines). The vertical projection is calculated between the dashed lines. The lower panels show interference patterns calculated for the pictured in-trap droplet configurations (green outlines). **a**, Linear chain of phase-coherent droplets, showing uniaxial modulation persisting in an averaged image (26 trials). **b**, Zigzag configuration of phase-coherent droplets, showing modulation along two directions that persists in an averaged image (51 trials), and hexagonal structure. The spacing of rows in the simulation was adjusted to approximate the observed aspect ratio of the TOF image. The image outlined in blue shows the average momentum distribution calculated from a series of 20 variational calculations converging to slightly different droplet configurations, showing the tendency of such fluctuations to broaden features in the interference pattern while maintaining the underlying structure. **c**, Zigzag configuration of phase-incoherent droplets. The modulation remains in single images, as evidenced by the spread of grey traces in projection, but disappears in the averaged image (43 trials). The data in **a** and **b**, **c** correspond to trap aspect ratios $\alpha_t = 0.30$ and $\alpha_t = 0.41$, respectively.

to independent droplets, and also calculate the averaged interference pattern for a zigzag state with the phases of the individual droplets randomized between simulated trials (Fig. 3c). In both cases, the averaged image does not show clear periodic modulation.

Conclusions

By exploiting the transition between linear and zigzag states, we have accessed a regime where the supersolid properties of periodic density modulation and phase coherence exist along two separate dimensions. Future work will focus on further understanding the spectrum of collective excitations in the full 2D system[26–28,43], where both the crystalline structure and the exchange of particles between droplets will have an important role. Further investigations may elucidate in more detail the nature of the phase transitions and expected configurations in a wider range of trap aspect ratios, as well as the role that defects have in the 2D system, either as phase slips in the zigzag patterns[44,45] or as vortices trapped between droplets of the array[29–31].

Online content

Any methods, additional references, Nature Research reporting summaries, source data, extended data, supplementary information, acknowledgements, peer review information; details of author contributions and competing interests; and statements of data and code availability are available at https://doi.org/10.1038/s41586-021-03725-7.

1. Gross, E. P. Unified theory of interacting bosons. *Phys. Rev.* **106**, 161–162 (1957).
2. Gross, E. P. Classical theory of boson wave fields. *Ann. Phys.* **4**, 57–74 (1958).
3. Andreev, A. F. & Lifshitz, I. M. Quantum theory of defects in crystals. *Sov. Phys. JETP* **29**, 1107–1114 (1969).
4. Chester, G. V. Speculations on Bose–Einstein condensation and quantum crystals. *Phys. Rev. A* **2**, 256–258 (1970).
5. Leggett, A. J. Can a solid be "superfluid"? *Phys. Rev. Lett.* **25**, 1543–1546 (1970).
6. Chan, M. H.-W., Hallock, R. & Reatto, L. Overview on solid ⁴He and the issue of supersolidity. *J. Low Temp. Phys.* **172**, 317–363 (2013).
7. Lu, Z.-K., Li, Y., Petrov, D. S. & Shlyapnikov, G. V. Stable dilute supersolid of two-dimensional dipolar bosons. *Phys. Rev. Lett.* **115**, 075303 (2015).
8. Baillie, D. & Blakie, P. B. Droplet crystal ground states of a dipolar Bose gas. *Phys. Rev. Lett.* **121**, 195301 (2018).
9. Roccuzzo, S. M. & Ancilotto, F. Supersolid behavior of a dipolar Bose–Einstein condensate confined in a tube. *Phys. Rev. A* **99**, 041601 (2019).
10. Boninsegni, M. & Prokof'ev, N. V. Colloquium: Super-solids: what and where are they? *Rev. Mod. Phys.* **84**, 759–776 (2012).
11. Tanzi, L. et al. Observation of a dipolar quantum gas with metastable supersolid properties. *Phys. Rev. Lett.* **122**, 130405 (2019).
12. Böttcher, F. et al. Transient supersolid properties in an array of dipolar quantum droplets. *Phys. Rev. X* **9**, 011051 (2019).
13. Chomaz, L. et al. Long-lived and transient supersolid behaviors in dipolar quantum gases. *Phys. Rev. X* **9**, 021012 (2019).
14. Guo, M. et al. The low-energy Goldstone mode in a trapped dipolar super-solid. *Nature* **574**, 386–389 (2019).
15. Natale, G. et al. Excitation spectrum of a trapped dipolar supersolid and its experimental evidence. *Phys. Rev. Lett.* **123**, 050402 (2019).
16. Tanzi, L. et al. Supersolid symmetry breaking from compressional oscillations in a dipolar quantum gas. *Nature* **574**, 382–385 (2019).
17. Birkl, G., Kassner, S. & Walther, H. Multiple-shell structures of laser-cooled ²⁴Mg⁺ ions in a quadrupole storage ring. *Nature* **357**, 310–313 (1992).
18. Raizen, M. G., Gilligan, J. M., Bergquist, J. C., Itano, W. M. & Wineland, D. J. Ionic crystals in a linear Paul trap. *Phys. Rev. A* **45**, 6493–6501 (1992).
19. Fishman, S., De Chiara, G., Calarco, T. & Morigi, G. Structural phase transitions in low-dimensional ion crystals. *Phys. Rev. B* **77**, 064111 (2008).
20. Shimshoni, E., Morigi, G. & Fishman, S. Quantum zigzag transition in ion chains. *Phys. Rev. Lett.* **106**, 010401 (2011).
21. Hew, W. K. et al. Incipient formation of an electron lattice in a weakly confined quantum wire. *Phys. Rev. Lett.* **102**, 056804 (2009).
22. Mehta, A. C., Umrigar, C. J., Meyer, J. S. & Baranger, H. U. Zigzag phase transition in quantum wires. *Phys. Rev. Lett.* **110**, 246802 (2013).
23. Astrakharchik, G. E., Morigi, G., De Chiara, G. & Boronat, J. Ground state of low-dimensional dipolar gases: linear and zigzag chains. *Phys. Rev. A* **78**, 063622 (2008).
24. Ruhman, J., Dalla Torre, E. G., Huber, S. D. & Altman, E. Nonlocal order in elongated dipolar gases. *Phys. Rev. B* **85**, 125121 (2012).

25. Santos, L., Shlyapnikov, G. V. & Lewenstein, M. Roton-maxon spectrum and stability of trapped dipolar Bose–Einstein condensates. *Phys. Rev. Lett.* **90**, 250403 (2003).

26. Ronen, S., Bortolotti, D. C. E. & Bohn, J. L. Radial and angular rotons in trapped dipolar gases. *Phys. Rev. Lett.* **98**, 030406 (2007).

27. Wilson, R. M., Ronen, S., Bohn, J. L. & Pu, H. Manifestations of the roton mode in dipolar Bose–Einstein condensates. *Phys. Rev. Lett.* **100**, 245302 (2008).

28. Bisset, R. N., Baillie, D. & Blakie, P. B. Roton excitations in a trapped dipolar Bose–Einstein condensate. *Phys. Rev. A* **88**, 043606 (2013).

29. Gallemí, A., Roccuzzo, S. M., Stringari, S. & Recati, A. Quantized vortices in dipolar supersolid Bose–Einstein-condensed gases. *Phys. Rev. A* **102**, 023322 (2020).

30. Roccuzzo, S. M., Gallemí, A., Recati, A. & Stringari, S. Rotating a supersolid dipolar gas. *Phys. Rev. Lett.* **124**, 045702 (2020).

31. Ancilotto, F., Barranco, M., Pi, M. & Reatto, L. Vortex properties in the extended supersolid phase of dipolar Bose–Einstein condensates. *Phys. Rev. A* **103**, 033314 (2021).

32. Zhang, Y.-C., Maucher, F. & Pohl, T. Supersolidity around a critical point in dipolar Bose–Einstein condensates. *Phys. Rev. Lett.* **123**, 015301 (2019).

33. Li, J.-R. et al. A stripe phase with supersolid properties in spin–orbit-coupled Bose–Einstein condensates. *Nature* **543**, 91–94 (2017).

34. Léonard, J., Morales, A., Zupancic, P., Esslinger, T. & Donner, T. Supersolid formation in a quantum gas breaking a continuous translational symmetry. *Nature* **543**, 87–90 (2017).

35. Kadau, H. et al. Observing the Rosensweig instability of a quantum ferrofluid. *Nature* **530**, 194–197 (2016).

36. Ferrier-Barbut, I., Kadau, H., Schmitt, M., Wenzel, M. & Pfau, T. Observation of quantum droplets in a strongly dipolar Bose gas. *Phys. Rev. Lett.* **116**, 215301 (2016).

37. Chomaz, L. et al. Quantum-fluctuation-driven crossover from a dilute Bose–Einstein condensate to a macrodroplet in a dipolar quantum fluid. *Phys. Rev. X* **6**, 041039 (2016).

38. Wächtler, F. & Santos, L. Quantum filaments in dipolar Bose–Einstein condensates. *Phys. Rev. A* **93**, 061603 (2016).

39. Bisset, R. N., Wilson, R. M., Baillie, D. & Blakie, P. B. Ground-state phase diagram of a dipolar condensate with quantum fluctuations. *Phys. Rev. A* **94**, 033619 (2016).

40. Lavoine, L. & Bourdel, T. Beyond-mean-field crossover from one dimension to three dimensions in quantum droplets of binary mixtures. *Phys. Rev. A* **103**, 033312 (2021).

41. Sohmen, M. et al. Birth, life, and death of a dipolar supersolid. *Phys. Rev. Lett.* **126**, 233401 (2021).

42. Hadzibabic, Z., Stock, S., Battelier, B., Bretin, V. & Dalibard, J. Interference of an array of independent Bose–Einstein condensates. *Phys. Rev. Lett.* **93**, 180403 (2004).

43. Schmidt, J.-N. et al. Roton excitations in an oblate dipolar quantum gas. *Phys. Rev. Lett.* **126**, 193002 (2021).

44. Pyka, K. et al. Topological defect formation and spontaneous symmetry breaking in ion Coulomb crystals. *Nat. Commun.* **4**, 2291 (2013).

45. Ulm, S. et al. Observation of the Kibble–Zurek scaling law for defect formation in ion crystals. *Nat. Commun.* **4**, 2290 (2013).

Article

Methods

Experimental apparatus and protocols

Our experimental apparatus is described in detail in ref. [46]. Here we evaporatively prepare up to $N = 6.5(5) \times 10^4$ condensed ^{164}Dy atoms in a crossed optical dipole trap (ODT) formed at the intersection of two beams derived from the same 1,064-nm laser, but detuned in frequency to avoid interference. The condensate fraction is typically 35–45%, depending on the exact trap parameters. One beam (the static ODT) has an approximately 60-μm waist. The second (the scanning ODT) has an 18-μm waist, whose position can be rapidly scanned horizontally at 250 kHz to create a variably anisotropic time-averaged potential. By tuning the power in each beam, and the scanning range of the scanning ODT, we gain independent control of the trap frequencies in all three directions. The two trapping beams propagate in a plane perpendicular to gravity, and cross at a 45° angle, which leads to the rotation of the zigzag state at high α_t visible in Fig. 2b.

We apply a uniform magnetic field oriented along gravity and perpendicular to the intersecting dipole traps, with which we can tune the strength of contact interactions between atoms. This allows us to create unmodulated Bose–Einstein condensates, supersolid states or states consisting of independent droplets at fields of $B = 23.2$ G, $B = 17.92$ G and $B = 17.78$ G, respectively.

In-trap and TOF images are performed along the vertical direction (along B and gravity), using standard phase-contrast and absorption techniques, respectively, as described in ref. [41]. The resolution of our in-trap images is approximately 1 μm. We use a 36-ms TOF duration for imaging interference patterns.

Atom number

We extract the condensed atom number N from absorption imaging performed along a horizontal direction in a separate set of experimental trials under otherwise identical experimental conditions. This allows for a larger field of view and better fitting of thermal atoms. These absorption images feature a clear bimodal profile, with a broad component associated with thermal atoms, and a narrow feature associated with the (quasi)-condensate. As the shape of TOF interference pattern of the modulated state is not known ahead of time, we determine N by performing a two-component fit to the condensed and thermal atoms (using a Thomas–Fermi and Bose-enhanced Gaussian, respectively), then subtracting the fitted thermal component from the total absorption signal. Reporting the directly fitted condensed component produces similar results, even though the Thomas–Fermi profile does not precisely describe the TOF interference pattern of the modulated state.

Because of how we count atoms in the experiment, and because the variational theory only includes atoms contained within droplets (and not in the diffuse halo that surrounds the droplets), care must be taken in how N is defined when comparing between the three approaches. For the TOF procedure used in the experiment, we find from the eGPE simulation that the halo is repelled at early expansion times, and is probably indistinguishable from the thermal cloud in our TOF measurements. This means that the atom number measured in the experiment predominantly corresponds to those in the droplets. For purposes of comparison, we thus define N as the number of atoms contained within the droplets. The eGPE simulation thus includes more than N total atoms, with the excess (typically about 20% of the total) forming the halo. We exclude these halo atoms when comparing with the experiment (where they are probably not visible in our atom counting procedure) or with the variational model (where they are not present).

Scattering length

The positions of phase boundaries between different droplet configurations are quite sensitive to the scattering length a, which is not known with high precision in our range of magnetic fields. For all theory, we use a value of $a = 88a_0$, where a_0 is the Bohr radius, as this value provides good agreement between experiment and theory for the 1D-to-2D transition point.

Extracting critical aspect ratio

The critical aspect ratio α_t^* is extracted from the fit to the function $\alpha_a = \alpha_0$ for $\alpha_t < \alpha_t^*$ and $\alpha_a = \sqrt{\alpha_0^2 + b(\alpha_t - \alpha_t^*)^2}$ for $\alpha_t > \alpha_t^*$, where α_t^*, α_0 and b are fitting parameters.

Interference patterns

The predicted interference patterns of Fig. 3 are calculated by assuming free expansion of Gaussian droplets. In reality, the droplets are probably not Gaussian, and interactions during TOF expansion may modify the interference pattern. However, the droplet shape primarily effects the envelope of the interference pattern, which is not our primary interest here, and from eGPE simulations, we expect the effects of interactions to be minor, provided that the droplets become unbound in a time short compared with the TOF, which we verify by both looking at shorter TOFs and comparing the fringe spacing observed in TOF with that expected from the in-trap droplet spacing. The positions and size of the droplets are tuned to provide illustrative interference patterns.

Droplet number

We extract the droplet number from our in-trap images using a peak-finding algorithm applied to smoothed images. The algorithm finds the local maxima above a threshold, which is chosen to be 40% of the overall peak value. Each in-trap density distribution is classified as linear array or 2D zigzag based on the atomic aspect ratio. Finally, the counts with a given droplet number are normalized by the total number of trials to obtain the probability shown in Fig. 2d. Fluctuations in the number of atoms in a given trial can push droplets above or below the threshold value, contributing to the spread in extracted droplet number for a given α_t.

Simulations

Our eGPE simulation is described in ref. [47]. Particles interact via contact interactions, characterized by the scattering length a, and dipole–dipole interactions, given by the dipole moment μ. Our eGPE calculations contain these two interactions, which enter the equation as $gn(\mathbf{r}) + \int d^3r' V_{dd}(\mathbf{r} - \mathbf{r}')|\psi(\mathbf{r}')|^2$, with $g = 4\pi\hbar^2 a/m$ the interaction coupling constant, $n(\mathbf{r})$ the local density and $V_{dd}(\mathbf{r})$ the dipole–dipole interaction. $\hbar$ and m represent the reduced Planck constant and the atomic mass, respectively. Beyond-meanfield effects are treated through the inclusion of a Lee–Huang–Yang correction term $\Delta\mu[n(\mathbf{r})] = \frac{32g}{3\sqrt{\pi}}\mathcal{Q}_5(\varepsilon_{dd})(n(\mathbf{r})a)^{3/2}$, where we take the real part of the auxiliary function $\mathcal{Q}_5(\varepsilon_{dd})$ defined in ref. [48]. $\varepsilon_{dd} = \frac{\mu_0\mu^2 m}{12\pi a\hbar^2}$, where μ_0 is the vacuum permeability, characterizes the strength of dipole–dipole interactions relative to contact interactions.

In the variational calculation, the energy of the droplet array depends on these interactions and the confinement. In particular, the energy of the array contains three contributions: first, the internal energy of each droplet, set by the combination of the interactions described above and kinetic energy. The internal energy is a function of the number of particles in the droplet, N_j, and determines the widths ($\sigma_{\rho(z),j}$) and the shape of the droplets (given by the exponents $r_{\rho(z),j}$). Second, the centre-of-mass energy of the droplet in the harmonic confinement, which depends on the positions x_j and y_j of the droplets. Third, the interdroplet interaction. The interaction between two droplets, j and j', may be well approximated by a function of the form: $\frac{V_{jj'}N_jN_{j'}}{(r_{jj'} + b_{jj'})^3}$, where $V_{jj'}$ and $r_{jj'}$ depend on the number of particles N_j and $N_{j'}$ in the droplets. The functions $V_{jj'}$ and $r_{jj'}$ are determined from fitting the interdroplet interaction (which is a relatively complicated integral expression) to the above-mentioned relatively simple functional form. We have checked that the fitting is excellent.

We minimize the overall energy with respect to the positions $\{x_j, y_j\}$ and the number of particles N_j in each droplet, constrained by the condition $N = \sum_j^{N_D} N_j$.

Linear-to-zigzag transition in Fourier domain

A state with 2D supersolidity must exhibit periodic density modulation as well as phase coherence along two dimensions. The former criteria (although also apparent from in-trap images) can be clearly verified in the Fourier domain, as shown in Extended Data Fig. 1. The top row shows the same in-trap images as in Fig. 2b, whereas the bottom row shows the average absolute value of the Fourier transform: $\langle|\mathcal{F}[n(x, y)]|\rangle$, where $\mathcal{F}$ is a 2D Fourier transform, $n(x, y)$ is the in-trap density profile extracted from images, and the average is taken over all images for a given trap (approximately 20 images for each condition). This clearly shows the transition from a state with modulation along a single direction for the linear chains, to a state with modulation along two dimensions for the zigzag state. Further, for the zigzag states, the hexagonal structure present in the Fourier transforms matches the triangular structure present in the in-trap images and the hexagonal structure present in the interference patterns shown in the main text (Fig. 3).

Prospects for bulk isotropic 2D systems

In the main text, we have focused primarily on the transition from a single row to a zigzag configuration—the minimal system that exhibits supersolid properties along two directions. However, such two-row configurations are not the limit of the 2D character possible in our system, and choosing an appropriate atom number and trap parameters can produce states with more than two rows. In principle, this could enable the production of bulk, isotropic systems, provided that a similar average atomic density is maintained. Here we present an experimental realization of configurations with more than two rows, as well as a theoretical investigation of the transition to an extended, isotropic 2D regime.

Experimental studies beyond two rows

The trap aspect ratio that we can achieve is limited to $\alpha_t \approx 0.43$ by the fact that the two beams that form our ODT do not cross at a right angle. Thus, we cannot access a configuration with more than two rows simply by further changing α_t. However, by decreasing the trap confinement in all directions near our maximum α_t, $(f_x, f_y, f_z) = (22(2), 55(2), 140(10))$ Hz, we observe the formation of states with more than two rows, as shown in Extended Data Fig. 2. In these looser trap configurations, the vertical trap frequency is critically sensitive to alignment of our two ODT beams, leading to variation over time and the large uncertainty in f_z.

In-trap images of these states show clear, periodic modulation along two directions (Extended Data Fig. 2a). This qualitative observation is confirmed by the average Fourier transform of the in-trap images, shown in Extended Data Fig. 2b, where distinct peaks indicate the presence of periodic modulation. The observed in-trap density profiles agree reasonably well with eGPE calculations of the ground state for these parameters, though our uncertainty in f_z allows for a range of exact configurations (the droplet configuration observed in Extended Data Fig. 2a, with nine clearly visible droplets, may suggest a slightly higher f_z and atom number than our most-likely independent estimates, used in the simulation of Extended Data Fig. 2c). Still, the eGPE results confirm that we do expect ground-state configurations with more than two rows of droplets for our experimental parameters.

In Extended Data Fig. 2d, we characterize the phase coherence of our extended state using TOF interference. The average TOF interference pattern, shown in the inset, features a bright central spot, surrounded by a lumpy ring. The structure of this ring is illustrated by the atomic density profile shown in the main panel, which is averaged over angle. The contrast between the interference pattern observed here and the clear hexagonal structure observed for the zigzag states in the main text may indicate an increased level of fluctuation, either in droplet phase or configuration, for the more extended system. This would

not be surprising, given that the atom numbers required to realize the extended states are at the edge of our experimental capabilities. Nonetheless, the clear ring shown in the averaged image and highlighted in the radial cut of Extended Data Fig. 2d indicates the presence of substantial phase coherence between droplets, as such a feature is not expected to be present in an incoherent droplet array.

Ground-state calculations beyond two rows

In Extended Data Fig. 3, we explore the transition from two rows to an isotropic system as a function of trap aspect ratio using the eGPE, in the regime beyond that currently accessible in our experiment (simply due to the beam layout dictated by technical constraints, and in some cases, atom number). To isolate the effects of trap geometry, we fix the average atomic density $N f_x f_y f_z$ to a value representative of our experimental conditions in high-aspect ratio traps. When we then also fix the trap volume by maintaining the product $f_x f_y$ and holding f_z constant (implying constant N), we find that a third row forms between $\alpha_t = 0.66$ and $\alpha_t = 0.82$. When the trap becomes round ($\alpha_t = 1$), the ground state is a symmetric hexagon with a droplet in the centre. Apart from our technical constraint on trap geometry, these conditions should be readily achievable in the experiment.

If instead we fix f_x and decrease f_y while increasing N (still holding the average atomic density fixed), we observe a transition from two rows to three and then more, as the number of droplets increases, eventually reaching symmetric hexagonal structure with 19 droplets (also predicted in ref. [8], for lower scattering length and higher trap frequencies) when $\alpha_t = 1$.

Importantly, the presence of the dilute background between the droplets, which is responsible for establishing and maintaining phase coherence, persists in the more extended systems. We quantify this in terms of the contrast $C = 1 - \frac{n_{\max} - n_{\min}}{n_{\max} + n_{\min}}$ where $n_{\max}$ and $n_{\min}$ are the maximum and minimum atomic density along a line connecting each pair of droplets, respectively. The reported C is the average over all pairs of adjacent droplets. We find that C decreases only slightly in the more extended systems (by 20% and 37% in the 7- and 19-droplet hexagons, relative to our 8-droplet zigzag state), indicating that such states would probably have similar coherence properties. This small change in contrast could also be compensated by a slight change in scattering length or trap frequencies.

Data availability

Data pertaining to this work can be found at https://doi.org/10.5281/zenodo.4729519.

Code availability

Code used for this work is available from the corresponding author upon reasonable request.

46. Trautmann, A. et al. Dipolar quantum mixtures of erbium and dysprosium atoms. *Phys. Rev. Lett.* **121**, 213601 (2018).
47. Chomaz, L. et al. Observation of roton mode population in a dipolar quantum gas. *Nat. Phys.* **14**, 442–446 (2018).
48. Lima, A. R. P. & Pelster, A. Quantum fluctuations in dipolar Bose gases. *Phys. Rev. A* **84**, 041604 (2011).
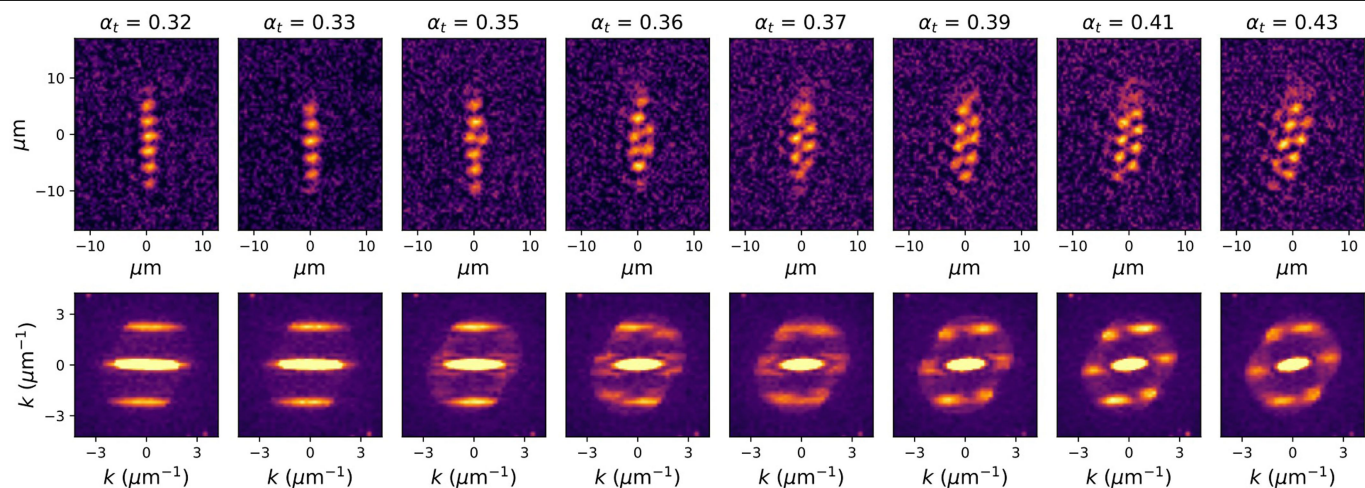
Article

Competing interests The authors declare no competing interests.

Additional information
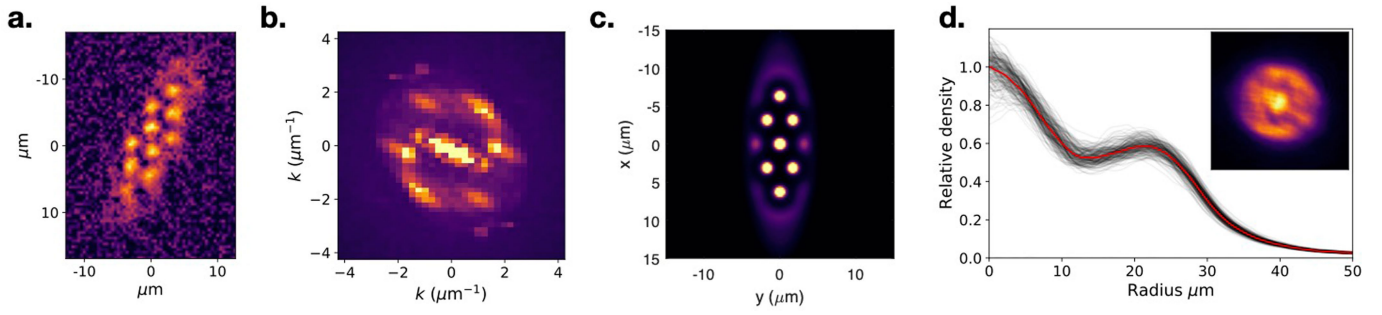**Correspondence and requests for materials** should be addressed to F.F.
Peer review information *Nature* thanks the anonymous reviewers for their contribution to the peer review of this work.
Reprints and permissions information is available at http://www.nature.com/reprints.
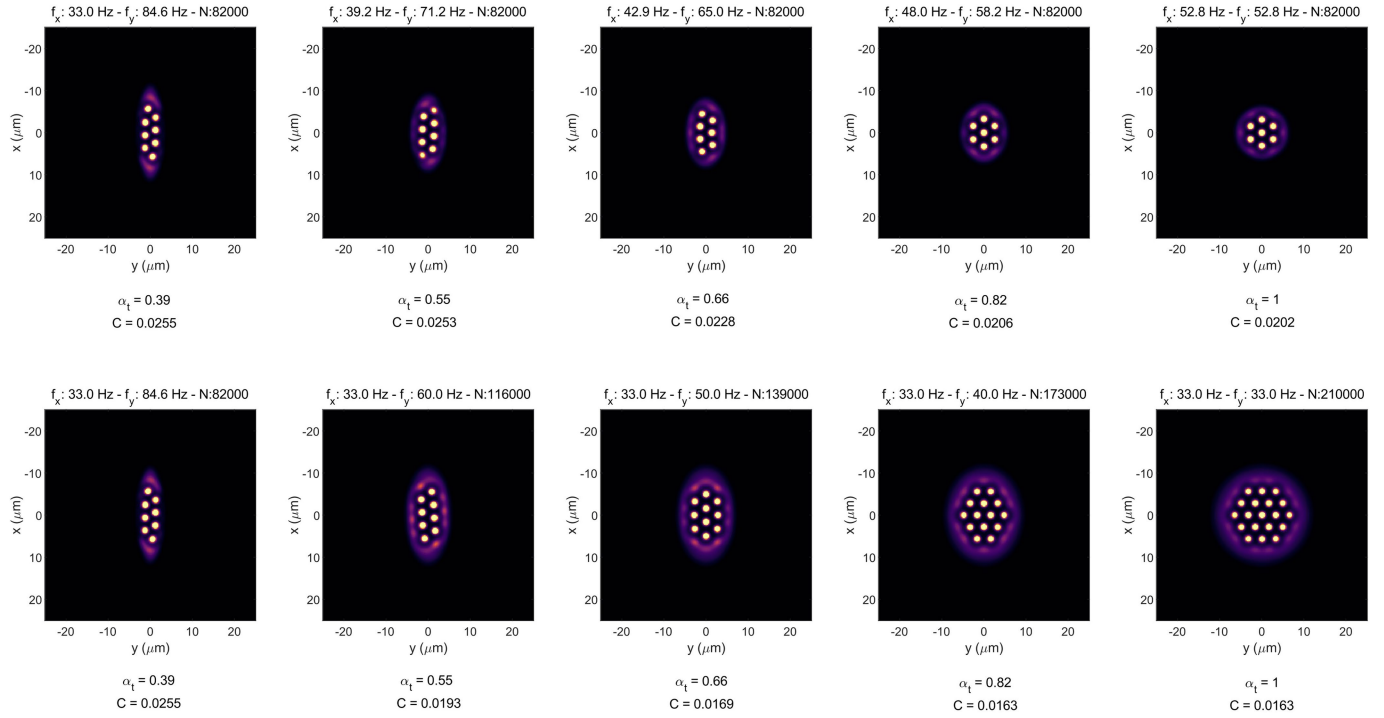
Extended Data Fig. 1 | Fourier transforms of in-trap images. The upper row shows individual in-trap images for different trap aspect ratios, as shown in Fig. 2b. The lower row shows the data for the same parameters in the Fourier domain, with k the associated wavenumber. As the trap aspect ratio is increased, the modulation goes from being present along a single direction to two, and a clear hexagonal pattern is visible.

a.

b.

c.

d.

Extended Data Fig. 2 | Supersolid droplet array with more than two rows.
a, In-trap image of a droplet array with more than two rows. **b**, Averaged Fourier transform of 309 images in conditions of **a**, showing that a regular modulated structure persists in the more extended system. **c**, Calculated ground state from the eGPE for trap parameters $(f_x, f_y, f_z) = (22, 55, 140)$ Hz, and $N = 60,000$ atoms in the droplets, representative of the experimental conditions in **a**, **b**.

d, Averaged TOF interference pattern for the conditions of **a**, **b**. The inset shows the measured 2D density profile and the main panel shows a radially averaged density, normalized to the peak density of the averaged image. The grey lines represent individual trials and the red line is the average. The repeatability of the modulation indicates the presence of phase coherence between droplets.

Extended Data Fig. 3 | Prospects for larger and isotropic droplet arrays. The panels show eGPE-calculated ground-state density profiles with fixed average atomic density (see text) and either fixed atom number and trap volume (upper row) or fixed f_x (lower row). Here N refers to the total number of atoms in the simulation (droplets plus halo), in contrast to the definition used elsewhere to compare with experimental conditions (droplets only).